LLNL-JRNL-857094

LAWRENCE LIVERMORE NATIONAL LABORATORY

Real time tracking of CO2 concentration using an optical microsphere resonator sensor

B. J. Demory, L. Echeveria, C. Tolfa, S. Sahota, V. Khitrov, A. S-P. Chang, T. Bond

November 10, 2023

Applied Spectroscopy

Real time tracking of CO_2 concentration using an optical microsphere resonator sensor

Brandon Demory[1], Logan Echeveria[1], Christian Tolfa[1], Sara Harrison[1], Victor Khitrov[1], Allan S.P. Chang[1], Tiziana Bond[1]*

[1]*Lawrence Livermore National Laboratory—7000 East Avenue, Livermore, CA, USA 94550*

*Corresponding Author: Tiziana Bond, Bond7@llnl.gov

Abstract

Whispering gallery mode resonator sensors are nondisruptive optical sensors that can detect and monitor perturbations in a gaseous environment. Through its resonant properties of peak wavelength, amplitude, and quality factor (Q factor), changes in concentration can be quantified within seconds and monitored over days with great stability. In addition, the small footprint, low cost, and high sensitivity are ideal properties for a disposable sensor that can be utilized in extreme environments. The large Q factor of the resonant cavity enables long interaction lengths and amplifies the effect of small changes in background refractive index, which is detectable in picometer shifts of the resonance wavelength. However, this measurement is susceptible to changes in other environmental factors such as temperature, pressure, and humidity, which manifest on the picometer wavelength scale, reinforcing the need to decouple the variables. In this work, we compare the spectral response of different diameter resonators to Carbon Dioxide, Nitrogen, and its mixtures, observing the spectral shifting and broadening of the cavity resonance near 1550nm. In addition, the effect of environmental temperature on spectral shifting due to the thermo-optic effect is characterized and quantified. Lastly, the gas concentrations are changed in real-time to showcase the tracking and recovery capabilities of the resonator sensor.

Keywords

Absorption spectroscopy, Real time, Resonator, Microsphere, Gas sensor, Detection

Introduction

The increasing demand for sensors capable of real-time gas storage monitoring and leak detection for gases such as Carbon Dioxide (CO_2), methane, and geological Hydrogen (H_2) has driven the growth of nondisruptive, optical based sensors.[1, 2] Whispering Gallery Mode Resonators (WGMRs) are ideal sensor candidates due to their small size and footprint, low manufacturing cost, and reusability.[3-5] Optically, they have high power densities, high quality factors (Q factor), and spectrally narrow resonances; furthermore, silica microspheres also show low material absorption.[1, 5] To date, there are many experiments showcasing the detection capabilities of WGMRs, in both fiber microspheres and on-chip resonators,[6] illustrating the application bandwidth of the technology. The long light-analyte interaction lengths (≈cm’s) on the resonator surface allow for the detection of small index of refraction ($\Delta n/n < 10^{-4}$) changes in the environment.[4, 7, 8] In aqueous environments, the use of coatings or binding agents on the microsphere facilitates surface binding, causing wavelength shifts and amplitude dampening.[9, 10] This approach typically degrades reusability as the binding agent is depleted but ensures the specificity of the bound agent to the microsphere, improving sensor fidelity.[11] In gaseous environments, changing the composition of the gas is detectable through resonance wavelength shifts or amplitude changes due to resonant absorption of the emission leaking from the cavity.[12-14] However, regardless of the environment type, measurements using WGMRs are susceptible to changes in standard temperature, humidity, and pressure. Deviations in these factors from their initial values induce resonant wavelength shifts on the picometer scale in a CO_2 environment. This is the same order of magnitude as the wavelength shift due to changing gas composition. Therefore, it is important to characterize these standard factors independent of resonant absorption and refractive index changes to decouple their effect on the desired measurement.

Materials and Methods

In this work, we investigate the real-time tracking of CO_2 concentration using a WGMR microsphere sensor. The paper is broken up into four components. First, the effect of microsphere diameter on the resonance shape and wavelength shift due to background index is quantified. This result dictates the diameter of the microsphere used for the remaining measurements. Next, the background temperature of the system is varied to determine the thermo-optic effect on the microsphere resonance wavelength. This is done at a wavelength far from the CO_2 absorption window to isolate the temperature effect from absorption heating. At this point, we acknowledge and estimate the shifts induced by humidity and pressure on the resonance position, as a full calculation is outside of the scope of this letter. Third, the resonance wavelength shift due to gas concentration is measured at steady state, varying from nitrogen (N_2) to CO_2. Finally, background index and resonance absorption are measured in real-time, varying the gas concentration over 180 minutes, with data taken every 10 seconds, to emulate live data monitoring.

Sensor Assembly

The WGMR sensor consists of a tapered waist fiber coupled together with a microsphere, placed on the end of a 1” piece of fiber. Both fibers are SMF-28 commercial off the shelf fiber from Corning. The microsphere is fabricated using arc pulses from a fusion splicer, which anneals the fiber tip into a sphere. The sphere diameter increases with the number of pulses. The tapered fiber is created by a CO_2 laser splicer, which heats and pulls the fiber until an adiabatic 4µm diameter waist taper is reached. The details of the fabrication procedure, including instrument specifics, are in prior published work.[15] The tapered fiber is mounted with epoxy onto a glass slide and connectorized with FC/APC connectors. The microsphere and tapered fiber are assembled using a custom aluminum mount, shown in Figure 1a, which controls the fiber gap. Using a Keyence optical microscope (VHS-7000), the microsphere’s height and in-plane position are adjusted until the microsphere is at the center of the tapered region and in contact. Contact between the microsphere and fiber ensures there is transmission into the microsphere at the expense of critical coupling.[16] An image of the coupled taper and a 100µm diameter microsphere, which is referred to as the microsphere sensor from here onward, is shown in Figure 1b. Once secured, the sensor does not need adjustment, as our current sensor has been in operation for two years without any damage or movement.

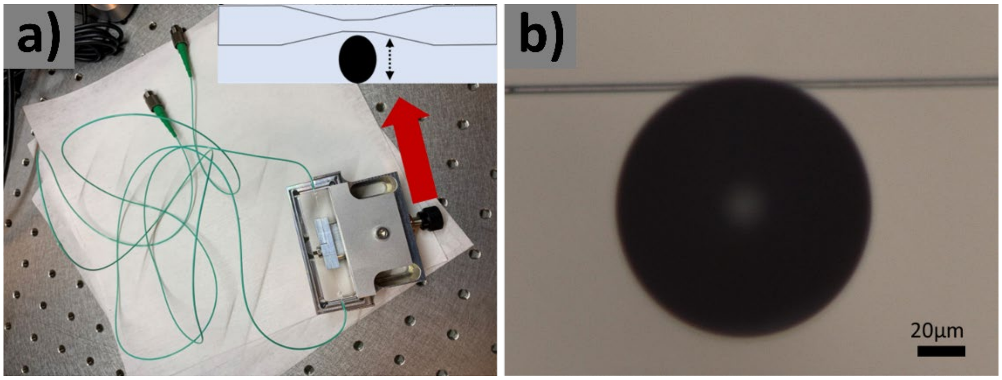

Theoretical Modeling

The WGMR microsphere was modeled in 2-D using Lumerical FDTD,[17] prior to measurement of the sensor. With a dipole source located within the edge of the circular resonator, the wavelengths of the optical resonances that satisfy the path length equation:

$$\pi \mathrm{n} \mathrm{D} = \mathrm{m} \lambda \tag{1}$$

can be calculated, where, n, is the index of refraction of the resonator, D, is the resonator diameter, m, is the resonance order, and λ, is the resonance wavelength. Two dipoles were included, with E-field orientation perpendicular and parallel with respect to the side of the sphere, to capture both TE and TM modes. The wavelength range of interest is 1570nm-1580nm, which overlaps with the CO_2 near-infrared (IR) absorption band.[18] The refractive indices used for the silicon dioxide SiO_2 microsphere, background air, and background CO_2 are 1.4437, 1.00, and 1.00044, respectively.[19] For a 40µm sphere, m is approximately 115 and there is a resonance around 1572.239nm. The simulation was run for N_2 and CO_2 backgrounds to calculate the magnitude of the resonance shift. For the 40µm sphere, there is a peak red shift of 8 picometers, as shown in Figure 2a, which is well within our detection capability. We repeated the simulation for 100µm, 200µm, and 250µm diameter spheres, to determine the diameter effect on resonance shift. In Figure 2b, we plot the microsphere diameter versus resonance wavelength shift due to the changing background index. The dotted line represents a piecewise cubic interpolation of the four values to illustrate the nonlinear relationship between the parameters. As the resonator diameter increases, the magnitude of the shift in wavelength decreases. This is due to an increase in the electric field confinement with increasing sphere size, reducing the influence of the change in background index of refraction on the resonance wavelength.

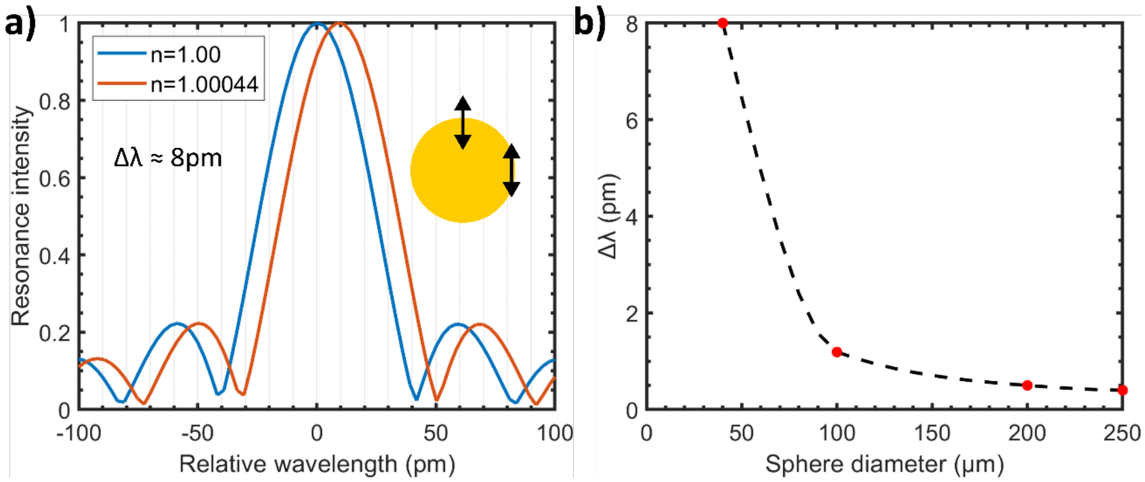

A smaller diameter resonator is ideal as it is more responsive to changes in the gas index of refraction than a larger diameter sphere. However, smaller diameter microspheres have fabrication and measurement trade-offs. As the target diameter of the sphere is decreased, the fabrication difficulty increases, as it is challenging to reliably make a ≤40µm diameter microsphere from standard 125µm diameter SMF-28 fiber using the splicer heating method without reducing the starting diameter of the fiber through tapering first. Optically, it is harder to overlap the resonance of a smaller sphere with the CO_2 absorption band. The free spectral range (FSR):

$$\Delta\lambda = \frac{\lambda^2}{\pi \mathrm{nD}} \tag{2}$$

which is the spacing between same order resonances, is inversely proportional to diameter. For a 40µm sphere, there is at most one first order resonance within the 10nm wide absorption band as the FSR is ≈14nm, and the FSR will grow with smaller diameters, worsening the chance of spectral overlap with gas absorption lines. Plus, the imperfections in the sphere shape from splicer heating are more pronounced at smaller diameters, reducing the Q factor of the resonances and sensitivity of the sensor. Therefore, we targeted microsphere diameters of 100µm for the gas detection experimental measurements. Due to the simplicity of the fabrication procedure and low cost of supplies, we can be ultra selective on the types of spheres being used, ensuring we have a uniform sphere with high enough Q factor for measurements. For a 100µm diameter sphere, the fusion splicer variation is about 100µm +/- 10µm, and the FSR is ≈5.5nm. This creates the possibility of 2 first order resonances within the 10nm wide absorption band, improving the chances of absorption band overlap.

Experimental Design

A schematic of the spectroscopy setup is in Figure 3a. A (New Focus Velocity TLB-6700) tunable IR laser (1550nm-1625nm) with programmable wavelength scanning, set to 1mW output power, is used as the excitation source for the measurement. To focus on individual resonances, a function generator is used to fine tune the laser wavelength +/-150pm around the set wavelength. The laser signal is split through a polarization maintaining (PM) 90%:10% power splitter, with the signal arm (90%) connected to the gas cell optical input and the reference arm (10%) sent through a fiber-coupled CO_2 filled reference cell (Wavelength References) to monitor the CO_2 absorption peak wavelength positions. The gas cell, pictured in Figure 3b, is vacuum sealed with optical pass-through connections to the sensor inside and a detector at the output. PM 1550nm patch cables were used to make all intermediate connections. The detectors are commercially available TEC cooled InGaAs amplified photodetectors (Thorlabs APD130C). The laser wavelength output and the two detector signals are fed into an oscilloscope for synchronous detection of all signals, with data collection driven by Labview. Mounted inside the gas cell is a (CO2 Meter ExplorIR) 0%-100% CO2 sensor (ExplorIR) that monitors the temperature and CO_2 concentration, which we used to validate our setup. The gas cell is placed inside a temperature-controlled chamber to control room temperature variations. Ball valves are placed on the gas cell intake and exhaust ports to stop gas flow as needed.

The tested gas cell leak rate is negligible (≈1% concentration change over a few hours). This was checked by sealing the gas cell with 100% CO_2 and monitoring the CO_2 concentration over time with the gas valves closed. After a few hours of no gas flow (≈8hrs), there is ≈5% relative humidity that is detected by the ExplorIR sensor inside the gas cell. The source of the imperfect seal is the feedthrough of the USB connections of the ExplorIR through the top port of the gas cell. The ambient air, typically containing between 20% - 70% relative humidity, of the temperature chamber can slowly seep into the gas cell when there is no positive pressure from gas flow. The nitrogen source is ultrahigh purity and dry and the CO_2 tank is pure. Throughout this work, the relative humidity inside the gas cell is monitored and measured to be 0%.

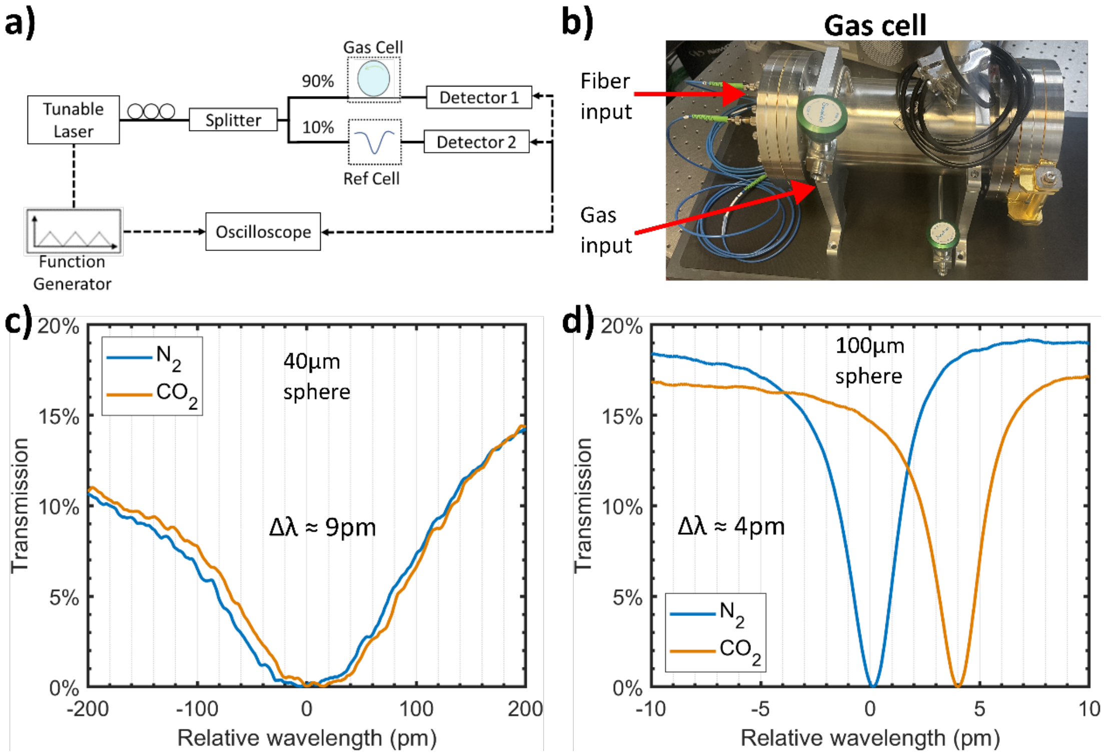

To verify the diameter dependent wavelength peak shift, we measured a 40µm and 100µm microsphere sensor independently in steady state conditions. For the steady state measurements, the temperature chamber is held at 25°C. The laser and temperature chamber are allowed to stabilize overnight to minimize fluctuations. The gas cell is purged with 5psi of N_2 for 1 hour to remove humidity and stabilize the starting N_2 environment for the sensor. After purging, the valves are closed on the gas cell and data acquisition is started after waiting 20 minutes to allow settling time for any vibrations or air currents. Data is recorded once a minute for 1 hour. Afterwards, the input gas is changed to CO_2 and flowed for 1 hour at 5psi, and the same process is repeated for the CO_2 measurement. The resonance wavelength is intentionally chosen away from the CO_2 absorption band to quantify the wavelength shift strictly due to refractive index change. Figure 3c shows the 40µm sensor agrees well with the simulated wavelength shift of 8pm. Here, the shift is measured from the center of the dip. The resonance is broader and less pronounced than the resonance measured with the 100µm sensor, seen in Figure 3d. The transmission amplitude differences between the two measurements are due to the transmission losses of the two fiber tapers used and the coupling losses of the different diameter microspheres. The wavelength shift is indiscriminate of the two λ(0)'s in Figure 3c and 3d, as the entire spectrum shifts. The measured wavelength shift of 4pm with the 100µm sensor is ≈3.3x the expected value of 1.2pm, which can be explained by diameter variations of the microsphere or coupling of the microsphere and taper at a perimeter less than the circumference. Because the microsphere and taper are manually aligned, the contact point may not lie at the equator. A shorter path length is equivalent to a smaller diameter sphere. Since a 4pm shift is well within our detection capability, we proceeded with the 100 µm sensor.

Results and Discussion

Thermo-Optic Effect

After the initial stability measurements to characterize the range of wavelength shift for this sensor, we examined the thermo-optic effect on the refractive index of the SiO_2 microsphere, N_2, and CO_2. The ideal gas limit is used to approximate the refractive index versus temperature for the gases,[20, 21] and the change in SiO_2 refractive index is ≈ 0.95×10^{-5} (RIU/°C).[22] Changes in microsphere diameter are excluded from this calculation, as the coefficient of thermal expansion is an order of magnitude smaller than the refractive index thermal coefficient.[23] Using FDTD, the change in the resonance wavelength peak was calculated in 5°C intervals from 10°C to 50°C for both gases. The average ($\Delta\lambda/\Delta T$) change for both N_2 and CO_2 is 10pm/°C, which agrees with theory.[23]

To verify the magnitude of the thermo-optic effect on the resonance peak shift, we changed the temperature of the gas cell with the sensor inside using the temperature-controlled chamber. A mass flow controller (MFC) set to 500sccm is used to constantly flow N_2 into the gas cell. To prevent condensation in the chamber, the temperature was limited to the range of 15°C - 25°C for this test. Once the chamber was initially stabilized at 15°C, data was taken in 5°C intervals at 15°C, 20°C, 25°C, 20°C, and again 15°C to confirm consistency. Resonance peak wavelength and temperature are recorded every minute for 1 hour. Then, the temperature is changed to the next setting and held for 30 minutes before the next 1 hour of data is recorded. This procedure was repeated for CO_2 the next day. The resonance wavelength peak versus gas cell temperature is shown in Figure 4a for N_2 and Figure 4b for CO_2, in a wavelength range outside of the absorption band. Although the chamber was given 30 minutes of settle time after temperature change, the temperature was still approaching setpoint equilibrium during the hour of data collection. There is an offset of 2°C between our oven setpoint temperature and the temperature read by the ExplorIR sensor, which is accounted for in Figure 4. Both N_2 and CO_2 corroborated the temperature response with simulation and theory,[23] producing shifts of 9.9pm/°C and 10pm/°C, respectively. This result reduces the complexity for real time measurements by understanding a variable on the resonance wavelength.

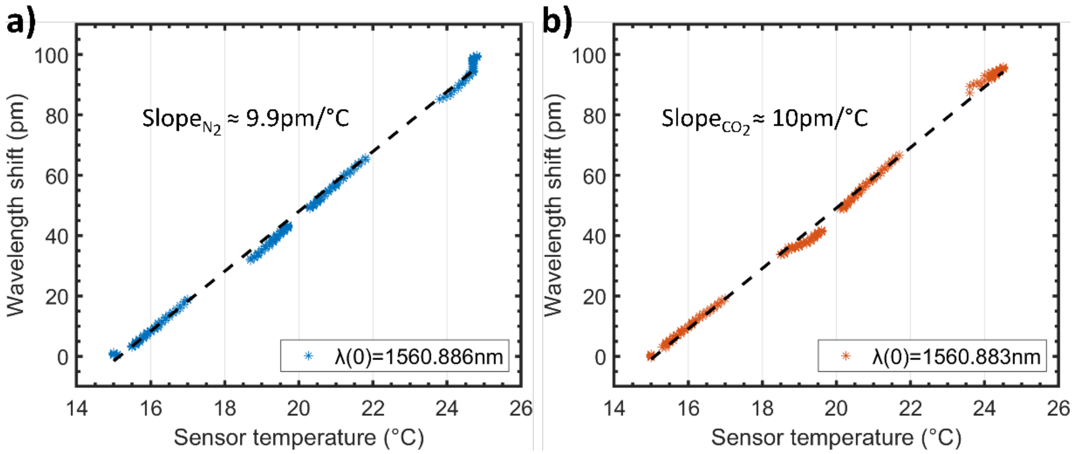

Humidity and Pressure

In addition to the temperature stability tests, we examined the effects of humidity and pressure independently on the resonance wavelength. To introduce humidity into the system, water vapor was mixed with nitrogen using MFCs. With the chamber set to 15°C, the gas cell was purged with N_2 to reduce the relative humidity of the cell to 0%. Then, 400sccm of N_2 gas was mixed with 100mg/h flow of water vapor into the gas cell. This resulted in a change in relative humidity inside the gas cell from 0% to 30% over 20 minutes. The resonance wavelength blue shifted less than 0.5pm over this period. So, for the 5% relative humidity we saw after the initial 3-hour leak test, the resonance wavelength should only blue shift by 83fm. Thus, we expect wavelength shifting due to the index of refraction change of the environment with the addition of water vapor;[24] however, additional characterization of this parameter is beyond the scope of this work.

To quantify the effect of changes in pressure on the resonance wavelength, a comparison of the HITRAN[18] CO_2 resonance peaks to the Wavelength References CO_2 cell resonance peak position is used. Pressure induced peak shift is given by the equation:

$$\tilde{\nu}^* = \tilde{\nu} + \delta(p_{1atm}) * p \qquad (3)$$

where $\tilde{\nu}$ and $\tilde{\nu}^*$ are the wavenumber of the original and shifted spectral line transitions in (cm^{-1}), δ is the pressure shift in air of the line transition with respect to the vacuum transition wavenumber (cm^{-1}/atm), and p is pressure in atm.[18] For the CO_2 absorption lines, δ is negative; therefore, pressures higher than 1atm red shift the transition wavelength. The CO_2 reference cell contains CO_2 at a lower pressure of 500Torr (0.66atm). The absorption peak at 500Torr in the CO_2 cell is blue shifted by 0.55pm with respect to the CO_2 absorption peak measured in the gas cell at 1atm. Future studies on the humidity and pressure effects are needed to fully characterize the expected induced wavelength shifts.

Steady State Gas Mixtures

The next step in sensor efficacy testing is the detection of partial mixtures of gases at steady states. For partial mixes, N_2 and CO_2 lines are connected to independent MFCs to control the respective gas flows such that the sum of the two flow rates is 500sccm. The percentage CO_2 in the CO_2/N_2 mixture is defined as the CO_2 concentration. The temperature chamber is stabilized at 25°C for this measurement. The desired concentration of CO_2 is flowed for 30 minutes while the gas cell stabilizes at the concentration. Data is taken every 5 minutes for 75 minutes (15 points) after stabilization while the gas mixture continues to flow. Then, the concentration is adjusted, and the process is repeated. Changes in the setpoint concentration were made in 25% intervals up to 100% CO_2 and back down to 100% N_2. Finally, data points at 100% CO_2 and 100% N_2, for a total of 11 measurements groups over 19.25 hours, were included at the end to check consistency. The average of the 15 resonance wavelength measurements versus CO_2 concentration in each of the 11 groups is shown in Figure 5.

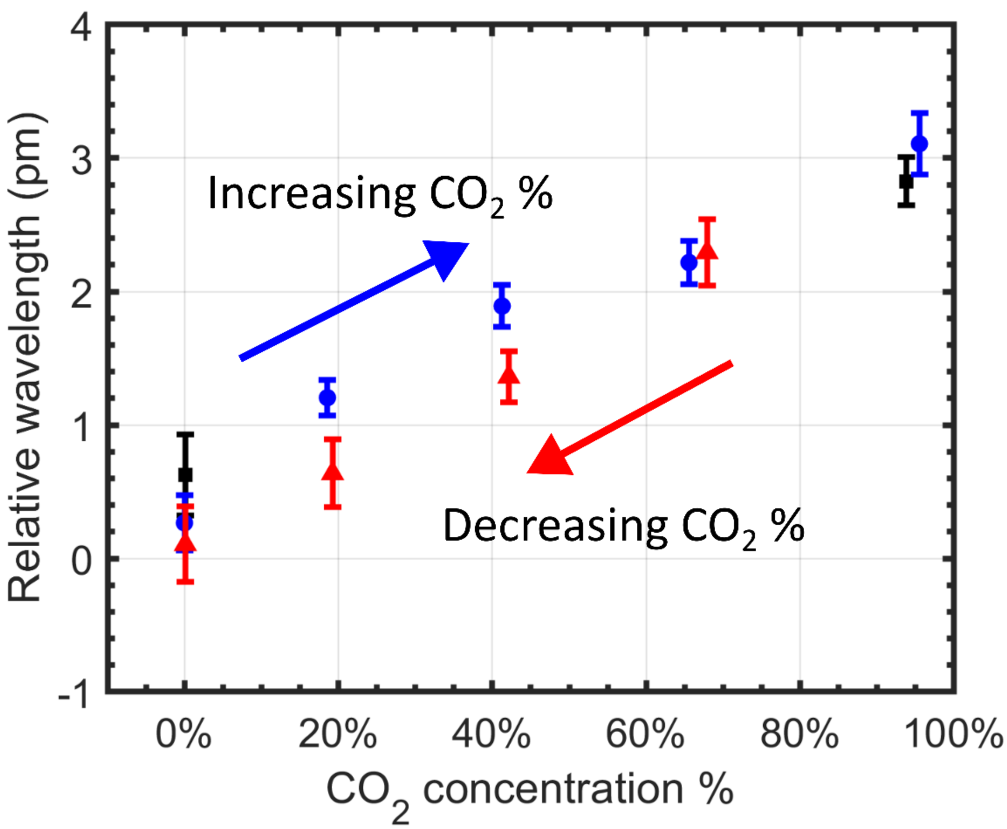

Starting at the resonance wavelength of 1560.289nm, there is a shift of 3pm from 100% N_2 to 100% CO_2 up to 1560.292nm, resulting in ≈0.3pm per 10% CO_2. However, within each of the 11 measurement groups, the standard deviation is on average ≈0.2pm. If we group the measurements by the setpoint concentrations, the spread is even larger. We attribute the spread to two factors. The first is that the tunable laser wavelength drifts over hours, which becomes obvious over the extended length measurements. The second factor is that 0.5pm is at the limit of the significant figures of our wavelength calculation. While the red shift trend is apparent and identifiable, sub picometer resolution would require modifications to the data collection and analysis procedure. Increasing the system resolution to better resolve the measurement-to-measurement variation is a subject for future work.

Real time Carbon Dioxide Absorption

Up to this point, we have shown the gas sensor mechanics decoupled from the gas absorption, as the gas absorption amplifies wavelength and temperature shifts. We examined the CO_2 resonance absorption band and introduced the real-time tracking of the CO_2 concentration by overlapping the gas flow and measurement intervals during the experiment. Flows of 500sccm, mixed concentration CO_2/N_2 are sent into the gas cell for 20 minutes followed by 20 minutes of 100% N_2 to purge the system. During the gas flow, measurements are recorded every 10 seconds. The gas flow procedures are repeated in 25% CO_2 concentration steps from 0% to 100% CO_2 for a total of 180 minutes, which should minimize laser wavelength drift due to the shortened experiment duration. This experiment was conducted at 15°C and repeated for both cases: on the CO_2 absorption resonance peak (on-absorption) and far from the CO_2 absorption band (off-absorption). To compare the two cases, we plot the shift from the initial wavelength position versus time, with CO_2 concentration on the second axis to illustrate when the gas flow changed, in Figure 6a. A rolling average of 50 wavelength measurements points is used to aid visual clarity. Starting at time 0 in 100% N_2 for 20 minutes, there is sub picometer jitter in the wavelength measurement, as the average wavelength blue-shifts slightly. As the gas mixture is changed to include carbon dioxide, the system responds to the change in background index, shifting the resonance wavelength. For low concentrations of CO_2, both cases behave similarly in wavelength shift. However, as the CO_2 concentration increases to 40%, we notice that the measurement on-absorption of CO_2 shows a larger wavelength shift. At the CO_2 absorption wavelength, the CO_2 gas is absorbing evanescent laser radiation, locally heating the sensor. The delta in wavelength shift is attributed to this absorptive heating. The heated sensor red shifts the resonance wavelength as demonstrated in Figure 4, which corresponds to a $\Delta T \approx 0.1°C$ - 0.2°C. While we cannot measure the temperature locally at the sensor to confirm ΔT, we have seen similar temperature increases with the introduction of CO_2 in the ExplorIR temperature sensor readout, which relies on IR absorption at a different CO_2 absorption peak wavelength.

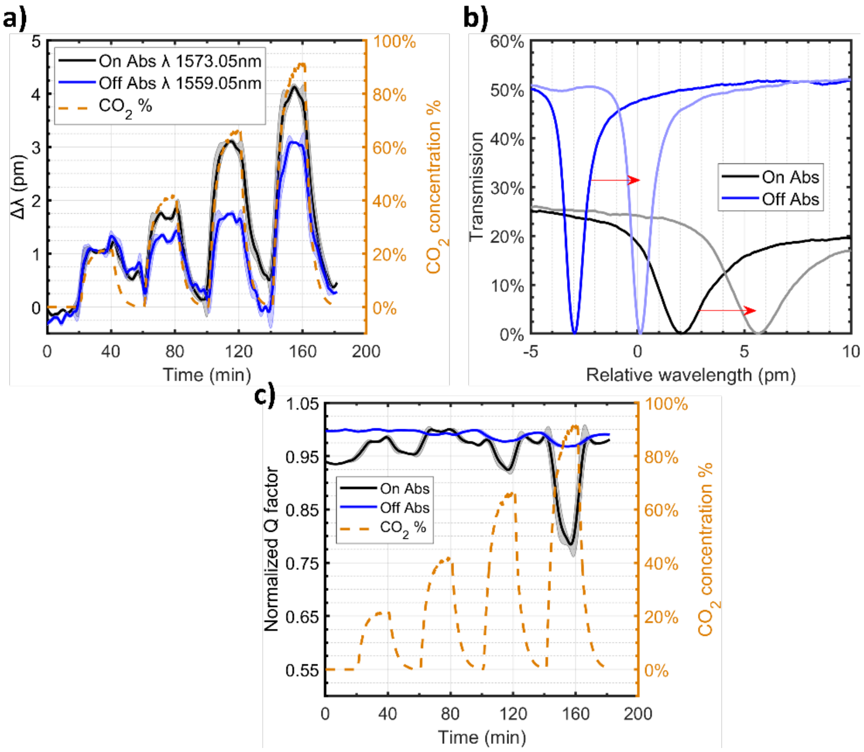

We also investigated the effect of CO_2 versus N_2 environment on the Q factor of the resonances. We compared the sensor resonance waveform in 100% N_2 at 140 minutes and 100% CO_2 at 160 minutes for both on (off) absorption in Figure 6b. While there is minimal change in the traces off-absorption, the on-absorption trace is visibly affected by the introduction of CO_2, becoming broader and having lower transmission. Verification of CO_2 absorption can be seen in the reduction of the Q factor of the resonance dip with gas change. We calculated the Q factor using MATLAB to generate a Lorentzian fit for each trace taken every 10 seconds and plotted the Q factor versus measurement time in Figure 6c. The shaded region represents the standard deviation of the smoothed average Q factor calculated using a moving average filter. For the off-absorption case, the magnitude of the Q factor is consistent throughout the 180-minute measurement, with a maximum deviation of ≤5% from the time=0 value ($1.58x10^6$), illustrating its gas independence. However, the on-absorption case, whose Q factor at time=0 is $4.7x10^5$, demonstrates gas dependent evolution. When the CO_2 concentration gets >50% around 120 minutes and 160 minutes, the CO_2 absorption is strong enough to induce local heating in addition to Q factor reduction. At 160 minutes, corresponding to the maximum CO_2 concentration, the drop in the Q factor from pure N_2 to CO_2 is ≈20%, almost 4x as large as the off-absorption case. The Q factor should decrease with increasing CO_2 concentration as the presence of more CO_2 gas increases the absorption local to the sensor, reducing the light transmission. However, both local sensor temperature and background refractive index affect the sensor's resonance wavelength peak position, while the CO_2 absorption wavelength peak does not move. So, we expect an ideal overlap condition (local temperature and CO_2 %) in which the sensor wavelength best overlaps the CO_2 absorption wavelength, maximizing the absorption. For our experimental conditions, the ideal wavelength overlap appears at 1573.087nm. This contributes to why the Q factor reduction at 120 minutes is modest versus 160 minutes, even though there is a significant CO_2 % in the chamber in both cases, as the sensor resonance wavelength is blue shifted 1pm from the ideal wavelength. With higher Q factor resonances, this effect will be more pronounced, and care must be taken to ensure the overlap of the CO_2 absorption wavelength and sensor resonance wavelength.

Sensor Sensitivity

To quantify the sensitivity of the microsphere sensor, we look at the resonance wavelength stability during the initial 20 minutes, in Figure 6a, in which the gas cell was purged with 100% N_2. For the constant gas concentration, the standard deviation of the resonance wavelength from its average value is +/-0.032pm. The "On CO_2 absorption" 0-100% dynamic range of our sensor is ≈4pm, which equates to a step size ($\Delta\lambda$ per % CO_2) of 0.04pm per 1% CO_2 concentration. Based on step size, the sensor accuracy is ≈+/-0.8% CO_2 or +/-8000ppm. This value is dependent on the Q factor of the sensor, which in this case is $\approx 10^5$, and it has been shown that Q factors on the order of (10^6 to 10^8) can improve the sensor accuracy down to (100's to 10's) of ppm.[12] In comparison to commercial off the shelf 0-100% range Nondispersive infrared sensors (NDIRs) such as the ExplorIR sensor used in this experiment, the typical accuracy of the CO_2 sensors is on the order of +/-(1%-5%) with response times of 10-30 seconds. The specification accuracy of our ExplorIR was +/-(300ppm + 5% of reading), which can be greater than 8000ppm for high CO_2 %. Better accuracy sensors are available at the expense of reduced dynamic range. Therefore, our sensor, which features a very large dynamic range (up to 100% CO_2), fast response time of ≈milliseconds (currently limited by laser tuning speed), and minimally invasive footprint is ideal for environments that may experience varying concentrations on short time scales.

Conclusion

In summary, we have demonstrated real-time tracking of CO_2 concentration using a microsphere-based absorption sensor. By monitoring the resonance peak position and Q factor over time, changes in CO_2 concentration can be detected. However, care must be taken to monitor temperature, humidity, and pressure. Using two sensors, one can maximize the capability of this detection scheme by taking advantage of the information available both inside and outside of the CO_2 absorption band simultaneously. The combination of the two sensors would verify temperature and gas concentration through wavelength shifts of the first sensor and amplitude shifts of the second sensor, without the need to deconvolve the absorption heating effect. This has direct application in monitoring the generation, storage, and destruction of greenhouse gases. Because of the fiber optical foundation, our sensor can be deployed remotely in unreachable or hazardous areas. Overall, the spectroscopy method employed by our sensor can be used for the detection of many different gaseous analytes such as water vapor, methane, oxygen, hydrogen, etc., in addition to aqueous targets, for an inexpensive, disposable, optical sensor.

Acknowledgements

This work was performed under the auspices of the U.S. Department of Energy by Lawrence Livermore National Laboratory under Contract DE-AC52-07NA27344. Lawrence Livermore National Security, LLC. LLNL-JRNL-857094.

ORCID iD

Brandon Demory https://orcid.org/0000-0002-9674-958X

References

1. J. Hodgkinson, R. P. Tatam. “Optical Gas Sensing: A Review”. *Meas. Sci. Technol.* 2012. 24: 012004.
2. E. Hand. “Hidden Hydrogen. Does Earth Hold Vast Stores of a Renewable, Carbon-Free Fuel?”. *Science*. 2003. 379(6633).
3. Y.-n. Zhang, T. Zhou, B. Han, A. Zhang, Y. Zhao. “Optical Bio-Chemical Sensors Based on Whispering Gallery Mode Resonators”. *Nanoscale.* 2018. 10(29): 13832-13856.
4. M. R. Foreman, J. D. Swaim, F. Vollmer. “Whispering Gallery Mode Sensors”. *Adv. Opt. Photonics.* 2015. 7(2): 168-240.
5. A. Matsko, A. Savchenkov, D. Strekalov, V. Ilchenko, L. Maleki. “Review of Applications of Whispering-Gallery Mode Resonators in Photonics and Nonlinear Optics”. *IPN Progress Report.* 2005. 42(162): 1-51.
6. T. M. Benson, S. V. Boriskina, P. Sewell, A. Vukovic, et al. “Micro-Optical Resonators for Microlasers and Integrated Optoelectronics”. In: S. Janz, J. Ctyroky, S. Tanev, editors. *Frontiers in Planar Lightwave Circuit Technology: Design, Simulation, and Fabrication.* Berlin, Germany: Springer. 2006. pp. 39-70.
7. G. C. Righini, Y. Dumeige, P. Feron, M. Ferrari, et al. “Whispering Gallery Mode Microresonators: Fundamentals and Applications”. *Riv. Nuovo Cimento.* 2011. 34: 435-488.
8. C. Ciminelli, C. M. Campanella, F. Dell’Olio, C. E. Campanella, M. N. Armenise. “Label-Free Optical Resonant Sensors for Biochemical Applications”. *Prog. Quantum Electron.* 2013. 37(2): 51-107.
9. J. L. Nadeau, V. S. Ilchenko, D. Kossakovski, G. H. Bearman, L. Maleki. “High-Q Whispering-Gallery Mode Sensor in Liquids”. Paper presented at: *High-Power Lasers and Applications.* San Jose, CA; Jan 20-Jan 25 2002. (4629) pp.172-180.
10. L. Labrador-Páez, K. Soler-Carracedo, M. Hernández-Rodríguez, I. R. Martín, et al. “Liquid Whispering-Gallery-Mode Resonator as a Humidity Sensor”. *Opt. Express.* 2017. 25(2): 1165-1172.
11. A. M. Armani, S. E. Fraser, R. C. Flagan. “Label-Free Single-Molecule All-Optical Sensor”. Paper presented at: *SPIE BIOS.* San Jose, CA; Jan 19-Jan 24 2008. (6852) pp.71-79.
12. A. T. Rosenberger, J. P. Rezac. “Whispering-Gallery-Mode Evanescent-Wave Microsensor for Trace-Gas Detection”. Paper presented at: *SPIE BIOS 2001 The International Symposium on Biomedical Optics.* San Jose, CA; Jan 20-Jan 26 2001. (4265) pp.102-112.

13. G. Farca, S. Shopova, A. Rosenberger. "Cavity-Enhanced Laser Absorption Spectroscopy Using Microresonator Whispering-Gallery Modes". *Opt. Express.* 2007. 15(25): 17443-17448.
14. Y. Sun, X. Fan. "Optical Ring Resonators for Biochemical and Chemical Sensing". *Anal. Bioanal. Chem.* 2011. 399: 205-211.
15. B. Demory, S. Harrison, C. Tolfa, L. Echeveria, et al. "Progress on Optical Microspheres for CO2 Sensors". Paper presented at: *SPIE LASE*. Online Only, CA; Mar 6-Mar 12 2021. (11672) pp.80-88.
16. M. Cai, O. Painter, K. J. Vahala. "Observation of Critical Coupling in a Fiber Taper to a Silica-Microsphere Whispering-Gallery Mode System". *Phys. Rev. Lett.* 2000. 85(1): 74.
17. Lumerical FDTD by ANSYS, http://www.lumerical.com.
18. L. S. Rothman, I. E. Gordon, Y. Babikov, A. Barbe, et al. "The HITRAN2012 Molecular Spectroscopic Database". *J. Quant. Spectrosc. Radiat. Transfer.* 2013. 130: 4-50.
19. A. Bideau-Mehu, Y. Guern, R. Abjean, A. Johannin-Gilles. "Interferometric Determination of the Refractive Index of Carbon Dioxide in the Ultraviolet Region". *Opt. Commun.* 1973. 9(4): 432-434.
20. E. R. Peck, B. N. Khanna. "Dispersion of Nitrogen". *JOSA.* 1966. 56(8): 1059-1063.
21. P. E. Ciddor. "Refractive Index of Air: New Equations for the Visible and Near Infrared". *Appl. Opt.* 1996. 35(9): 1566-1573.
22. C. Tan, J. Arndt. "Temperature Dependence of Refractive Index of Glassy SiO2 in the Infrared Wavelength Range". *J. Phys. Chem. Solids.* 2000. 61(8): 1315-1320.
23. G. Schweiger, M. Horn. "Effect of Changes in Size and Index of Refraction on the Resonance Wavelength of Microspheres". *J. Opt. Soc. Am. B.* 2006. 23(2): 212-217.
24. P. Schiebener, J. Straub, J. Levelt Sengers, J. Gallagher. "Refractive Index of Water and Steam as Function of Wavelength, Temperature and Density". *J. Phys. Chem. Ref. Data.* 1990. 19(3): 677-717.

Figure 1. a) Assembled sensor consisting of an adiabatically tapered SMF-28 fiber and a microsphere resonator. Using the adjustment knob, the microsphere to fiber gap is controlled. b) The 4µm taper and 100µm diameter microsphere are positioned in the same plane under magnification. The microsphere is brought into contact with the taper at the correct height.

Figure 2. a) Simulated first order resonance from a 40µm SiO_2 resonator in air (n=1.00) versus CO_2 (n=1.00044). The resonance peak at 1572.239nm red shifts 8pm due to the change in refractive index. The inset shows the orientations of the dipole sources within the resonator. b) The resonance peak shift versus microsphere diameter. Four points were simulated and connected by piecewise cubic segments.

Figure 3. a) Measurement system schematic. b) Photograph of the vacuum sealed gas cell containing the sensor. c) Comparison of N_2 versus CO_2 for a 40µm diameter sensor with $\lambda(0)$ of 1554.670nm. d) Comparison of N_2 versus CO_2 for a 100µm diameter sensor with $\lambda(0)$ of 1560.973nm.

Figure 4. Resonance peak wavelength versus gas cell temperature for a) N_2 and b) CO_2 environments. The linear fittings reveal a 9.9pm shift per 1°C for N_2 and a 10pm shift per 1°C for CO_2 with temperature. Measurements taken on different days.

Figure 5. Average Resonance Wavelength versus CO_2 concentration. The (blue) circles are during the ramp up of the CO_2 concentration. The (red) triangles are during the CO_2 concentration reduction. The (black) squares taken at the end of the measurement represent 100% N_2 and 100% CO_2. The error bars correspond to the standard deviation of the measured resonance wavelength over 75 minutes. The starting wavelength value λ(0) is 1560.289nm.

Figure 6. Magnitude of wavelength shift versus time for measurements on the CO_2 absorption peak wavelength and a wavelength far away from the absorption peak. Legend wavelengths indicate the respective starting wavelengths, λ(0). Measured CO_2 concentration versus time is overlayed to illustrate the gas transitions every 20 minutes. b) Comparison of the resonance waveform for N_2 at 140 minutes and CO_2 at 160 minutes near (far from) CO_2 absorption wavelength in black (blue). The starting wavelengths, λ(0), are 1573.084nm and 1559.947nm, respectively. The On (Off) absorption lines are displaced right 3pm (left 2pm) from zero for clarity. c) Normalized Q factor versus time for the resonance peak on-absorption and off-absorption in 6a. The Q factor at time=0 for on (off) absorption is 4.7×10^5 and 1.58×10^6, respectively. Reduction in Q factor occurs with higher CO_2 concentrations. In all plots, the shaded region is the standard deviation of the moving average fitting of the respective value.

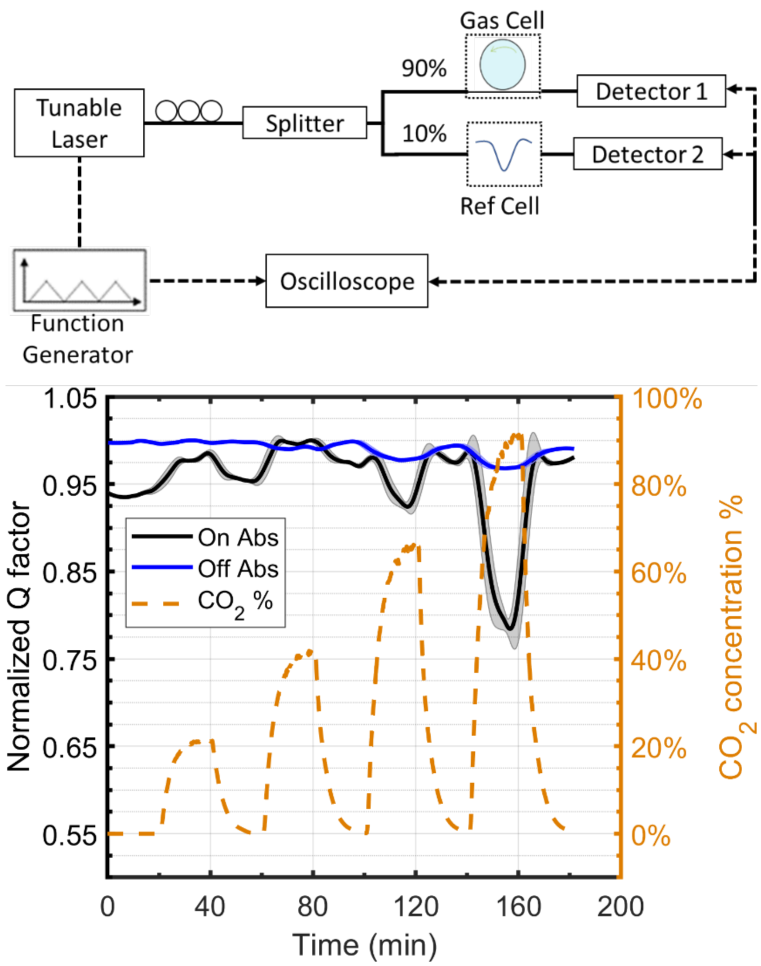

Graphical Abstract Figure Top: Schematic of optical setup used to compare real time changes in gas composition. Bottom: Real time tracking of the sensor's resonance wavelength for changing Carbon dioxide (CO_2) concentrations versus time both on and off the CO_2 absorption peak to illustrate the contributions of index of refraction and local gas heating.

LLNL-JRNL-857094